Assimilating Global Wave Model Predictions and Deep-Water Wave Observations in Nearshore Swell Predictions

SEAN C. CROSBY, BRUCE D. CORNUELLE, WILLIAM C. O'REILLY, AND ROBERT T. GUZA

Scripps Institution of Oceanography, La Jolla, California

ABSTRACT

Nearshore wave predictions with high resolution in space and time are needed for boating safety, to assess flood risk, and to support nearshore processes research. This study presents methods for improving regional nearshore predictions of swell-band wave energy (0.04–0.09 Hz) by assimilating local buoy observations into a linear wave propagation model with a priori guidance from global WAVEWATCH III (WW3) model predictions. Linear wave propagation, including depth-induced refraction and shoaling, and travel time lags, is modeled with self-adjoint backward ray tracing techniques. The Bayesian assimilation yields smooth, high-resolution offshore wave directional spectra that are consistent with WW3, and with offshore and local buoy observations. Case studies in the Southern California Bight (SCB) confirm that the nearshore predictions at independent (nonassimilated) buoy sites are improved by assimilation compared with predictions driven with WW3 or with a single offshore buoy. These assimilation techniques, valid in regions and frequency bands where wave energy propagation is mostly linear, use significantly less computational resources than nonlinear models and variational methods, and could be a useful component of a larger regional assimilation program. Where buoy locations have historically been selected to meet local needs, these methods can aid in the design of regional buoy arrays by quantifying the regional skill improvement for a given buoy observation and identifying both high-value and redundant observations. Assimilation techniques also identify likely forward model error in the Santa Barbara Channel, where permanent observations or model corrections are needed.

1. Introduction

Wind-generated gravity waves drive nearshore processes, including beach erosion, along- and cross-shore material transport, and oceanfront flooding, during high water levels. High-resolution nearshore wave predictions support beach and boater safety, coastal risk assessment, and nearshore process research. Wave prediction errors in coastal areas sheltered by islands and complex bathymetry are sensitive to details of offshore wave directions that are not well resolved by directional buoy observations (Ochoa and Delgado-González 1990) or global wave models (O'Reilly and Guza 1993; Rogers et al. 2007; O'Reilly et al. 2016). However, observations sheltered from varying directions can be included to increase resolution (O'Reilly and Guza 1998), similar to applications in acoustic and optics of inhomogeneous media (Borcea et al. 2002). Though current operational wave models—for example, Simulating Waves Nearshore (SWAN) or WAVEWATCH III (WW3)—do not yet

assimilate local wave observations, progress is being made. Recent developments (Veeramony et al. 2010; Orzech et al. 2013) use variational methodologies, relying on an adjoint model to propagate prediction misfits at local observation sites backward to the model boundary. An analytical adjoint (Walker 2006), developed originally for synthetic aperture radar satellite observations, has been extended to wave spectra (Veeramony et al. 2010); however, simulations were limited to linear wave processes (shoaling and refraction) and stationary conditions with homogeneous boundary forcing. Numerical methods have been developed to estimate an adjoint by linearizing the SWAN model (Orzech et al. 2013); however, initial tests are restricted to linear wave processes and stationary conditions. More recently, adjoint-free techniques have been developed, though initial testing has been restricted to synthetic data (Panteleev et al. 2015).

Linear wave propagation assumptions are valid for low-frequency wave energy in many nearshore regions where local fetch is limited and dissipation on a narrow shelf is negligible, for example, the Southern California Bight (SCB) (O'Reilly and Guza 1993; O'Reilly et al. 2016).

Corresponding author: Sean C. Crosby, sccrosby@ucsd.edu

However, in regions as large as the SCB ($\sim$350 km), propagation time lags reach 12 h and cannot be ignored (Rogers et al. 2007). Here, we present an alternative methodology for assimilating nearshore buoy observations that incorporates propagation time lags in a linear wave model. The preliminary analysis of O'Reilly and Guza (1998) (which includes time lags) is extended to include global wave model (GWM) predictions. A comparatively more general inversion framework is developed that incorporates observation uncertainty and a priori information. In contrast to recent assimilation work with SWAN, our alternative approach takes advantage of self-adjoint ray projection. Using historically underappreciated backward ray tracing techniques (Dorrestein 1960; Longuet-Higgins 1957), linear transfer coefficients between offshore and nearshore sites are generated. The resulting linear model and adjoint for wave energy propagation greatly reduce computational expenses compared with variational systems (Veeramony et al. 2010; Orzech et al. 2013) and allow for high spatial, temporal, and directional resolution. Our case studies with real buoy observations in the SCB show that inverted offshore wave conditions are plausibly smooth in time and direction, and that the assimilation of nearshore buoys increases the predictive skill at validation buoy sites not included in the assimilation.

This linear approach is limited to wave conditions, frequencies, and distances where dissipation and nonlinear spectral energy transfers are negligible. Offshore GWM predictions in Southern California (spatial scales of a few 100 km) suggest that linear wave propagation assumptions are valid for swell frequencies < 0.09 Hz, which contain 60% of the total offshore energy flux (Crosby et al. 2016, appendix A). Assimilation of higher-frequency observations requires more sophisticated techniques, more similar to current variational methodology (Orzech et al. 2013). However, the feasibility of representing nonlinear wind-wave growth, dissipation, and spectral energy transfers accurately in a numerically tractable model adjoint remains to be demonstrated.

An assimilation method is developed to estimate offshore directional spectra from directional and non-directional wave buoy spectral observations. The assimilation treats each frequency band independently, but it could be extended to use all frequency bands simultaneously because of the method's low computational costs. This would allow for assimilation of bulk parameters to the extent that non-swell-band energy is negligible (e.g., satellite altimeter observations and high-frequency radar during swell-dominated conditions).

Wave buoy observations are discussed in section 2, followed by details of the linear forward problem in section 3. The assimilation methodology (section 4) and

TABLE 1. Deep-water and shallow-water buoys site CDIP and NOAA identification numbers and mooring depth.

ID	CDIP ID	NOAA ID	Name	Depth (m)
Deep water				
D1	071	46218	Harvest	550
D2	107	46216	Goleta	182
D3	111	46217	Anacapa	114
D4	028	46221	Santa Monica	363
D5	092	46222	San Pedro	457
D6	096	46223	Dana Point	373
D7	045	46224	Oceanside	220
D8	100	46225	Torrey Pines	550
D9	093	46231	Mission Bay	201
D10	095	46226	Point La Jolla	181
Shallow water				
S1	131	—	Rincon Point	20
S2	141	46234	Port Hueneme	20
S3	118	—	Leo Carillo	20
S4	172	46230	Huntington Beach nearshore	20
S5	043	46242	Camp Pendleton	20
S6	155	46235	Imperial Beach	20

applications to synthetic and real observations (section 5) are followed by a discussion of the model constraints and implications for buoy array design (section 6). The paper concludes with a summary (section 7).

2. Observations

Hourly, quality-controlled Datawell low-order energy and directional buoy observations (Table 1) from the Coastal Data Information Program (CDIP, http://cdip.ucsd.edu) are smoothed in time with a 3-h running mean at each observed frequency. A comparison with a tower-mounted array of pressure sensors shows Datawell directional buoys accurately measure energy and four low-order directional moments (O'Reilly et al. 1996). At the ith buoy mooring location, at each frequency f, the observed moments $\tilde{\mathbf{y}}$ are related to the phase-averaged wave spectrum $E(f, \theta)$ by (Longuet-Higgins et al. 1963)

$$\tilde{\mathbf{y}}(i,f) = \begin{bmatrix} a_0(f) \\ a_1(f) \\ b_1(f) \\ a_2(f) \\ b_2(f) \end{bmatrix} = \begin{bmatrix} \int E(f,\theta)\,d\theta \\ \int E(f,\theta)\cos\theta\,d\theta \\ \int E(f,\theta)\sin\theta\,d\theta \\ \int E(f,\theta)\cos2\theta\,d\theta \\ \int E(f,\theta)\sin2\theta\,d\theta \end{bmatrix}. \quad (1)$$
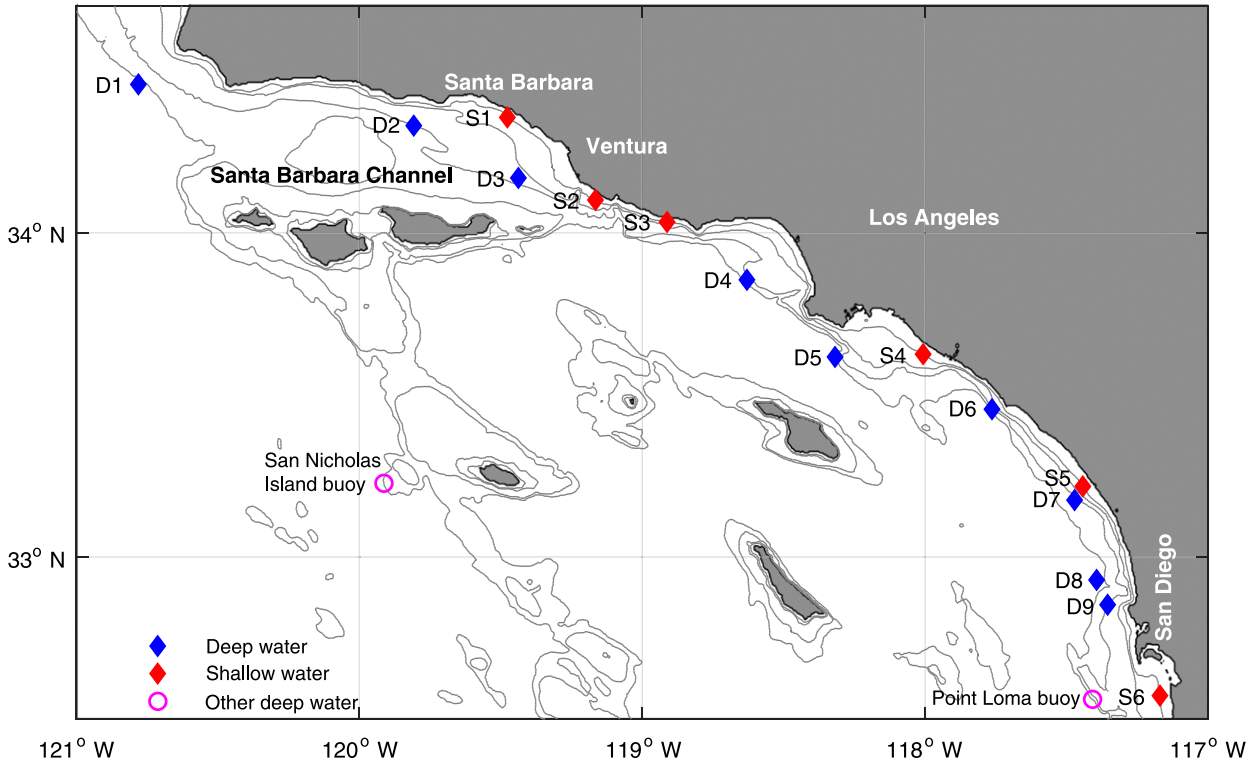
FIG. 1. SCB mooring locations of D and S, and other wave buoys operated by CDIP. Gray contours show 20-, 50-, 200-, and 500-m isobaths.

These integral moments, $\tilde{\mathbf{y}}$, of the directional wave spectrum can be transformed into several mean properties, for example, mean direction θ_m, directional spread, and others (Kuik et al. 1988), but they do not define a unique discrete directional spectrum (Ochoa and Delgado-González 1990; Crosby et al. 2016). Additionally, observed buoy moments contain statistical uncertainty owing to finite-length observation records (Long 1980; see also the appendix).

Buoy locations in the SCB (Fig. 1) were determined by user needs (e.g., harbor entrances) and logistics (e.g., mooring depth constraints). Shallow- ($\sim$20 m) and deep-water ($>$300 m) buoys are denoted by S# and D#, respectively.

3. Forward problem

In the SCB the continental shelf is narrow, and the swell wave forward model includes island sheltering and bathymetry-controlled refraction, and neglects wind generation, spectral energy transfers, wave–current interactions, and dissipation. These assumptions are justified by observations in the SCB (O'Reilly and Guza 1993; O'Reilly et al. 2016) and modeling studies in the Pacific Northwest (García-Medina et al. 2013), where the shelf is also narrow. Under these assumptions nearshore moments are linearly related to the offshore wave spectra E by

$$y(j,i,f) = \int K(j,i,f,\theta)E(f,\theta)\,d\theta, \qquad (2)$$

where K contains transfer coefficients for the observed moment j, location i, frequency f, and offshore direction θ.

Transfer coefficients are estimated by modeling refraction and shoaling using backward ray tracing techniques (Longuet-Higgins 1957; Dorrestein 1960). Ray propagation paths, traced following Snell's law as phase velocity changes with depth, are self-adjoint—that is, both forward and backward tracing will follow the same path. Advantageously, backward ray tracing sidesteps issues with caustics (Dorrestein 1960) and allows for rapid analysis for locations of interest. Here, rays are traced from nearshore buoy sites to deep-water offshore. Rays terminating at the coastline or offshore islands indicate blocked or sheltered directions, while those arriving at deep water indicate unsheltered directions. Temporarily ignoring energy travel time lags, from linear theory and geometric optics (Dorrestein 1960), transfer coefficients are estimated from the relation between initial and terminating ray angles,

$$\mathbf{K}(f,\theta^{(o)}) = \frac{c_g^{(o)}(f)}{c_g^{(n)}(f)} \iint \left| \frac{\Delta\theta^{(n)}}{\Delta\theta^{(o)}} \right| \mathbf{b}\,d\theta^{(n)}, \qquad (3)$$

where c_g is the group velocity, θ are ray directions, and (o) and (n) indicate offshore and nearshore properties, respectively. Terms $\Delta\theta^{(o)}$ and $\Delta\theta^{(n)}$ indicate the change in angle for adjacent rays terminating at the offshore and starting from the nearshore, respectively. The observing kernel **b** transforms to observed moments, and for directional buoy observations [(1)] is

$$\mathbf{b} = \begin{bmatrix} 1 \\ \cos\theta^{(n)} \\ \sin\theta^{(n)} \\ \cos2\theta^{(n)} \\ \sin2\theta^{(n)} \end{bmatrix}. \tag{4}$$

At sheltered locations the relationship between $\theta^{(o)}$ and $\theta^{(n)}$ can be complicated, for example, highly sheltered buoy D3 and moderately sheltered buoy D8 (Fig. 2a). Owing to refraction over shoals and island topography, waves with the same offshore direction can arrive at several nearshore directions (e.g., for D8 when $\theta^{(o)} = 230°$, $\theta^{(n)} = 230, 255, 285°$). Though $\theta^{(n)}$ versus $\theta^{(o)}$ is not monotonic, careful integration over discrete $\theta^{(o)}$ ranges of (3) can yield accurate transfer coefficients (Dorrestein 1960). For a fixed frequency, K contains many relatively narrow peaks and valleys (individual gray curves in Fig. 2b). Transfer coefficients are generated at fine frequency (0.0005 Hz) and directional ($<1°$) resolutions, and are averaged to 0.005 Hz, the buoy observational bandwidth for swell, and 1°, our desired directional resolution. The remaining finescale features, often with adjacent peaks and valleys (black in Fig. 2b), are blurred by the low-order moment-measuring buoys.

Hereinafter, (o) and (n) are dropped and θ now refers only to offshore wave directions. Additionally, the linear forward problem is solved independently at each frequency, and f is dropped for brevity. Nearshore directional buoy moments are related to offshore wave spectra by

$$\tilde{\mathbf{y}}(i) = \int \mathbf{K}(i,\theta)E(\theta)\,d\theta, \tag{5}$$

and discretized in direction, in matrix form, the forward problem becomes

$$\tilde{\mathbf{y}} = \tilde{\mathbf{H}}\mathbf{x}, \tag{6}$$

where transfer coefficients form the model kernel $\tilde{\mathbf{H}}$ with rows indicating buoy locations and measured moments, and columns indicating directions. The vector $\tilde{\mathbf{y}}$ comprises buoy observations at i locations, and the vector **x** is the offshore directional spectrum $E(\theta)$. Expected forward model error is not treated formally and will be absorbed into data misfit (section 5b). The model resolution matrix is $\text{res}(\tilde{\mathbf{H}}) = \tilde{\mathbf{H}}^{-g}\tilde{\mathbf{H}}$, where
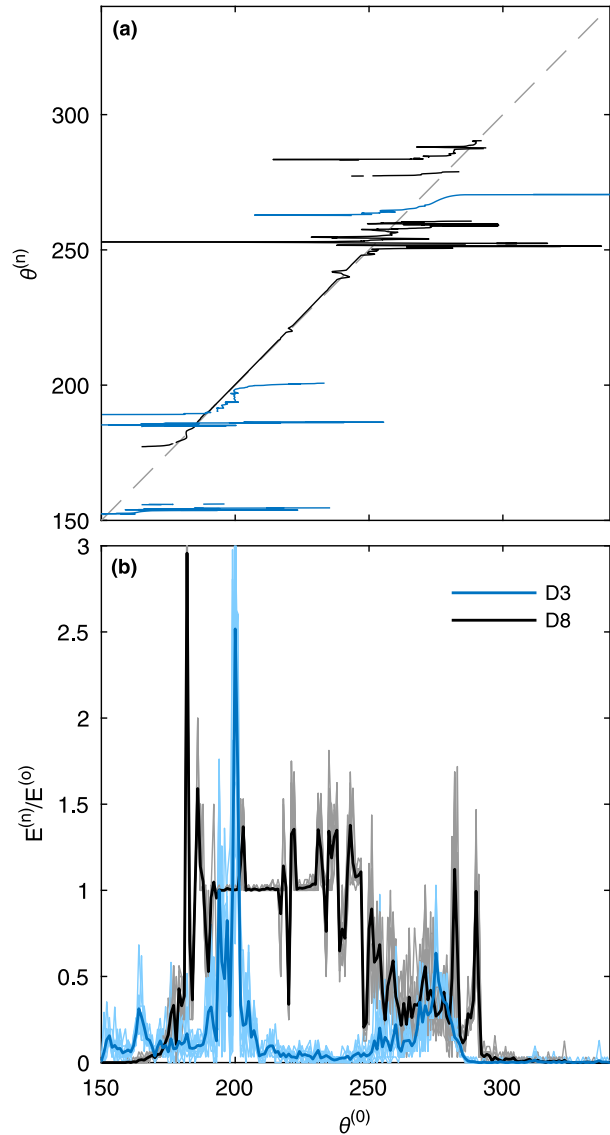

FIG. 2. (a) Nearshore ray angle vs offshore ray angle for 0.07 Hz. Rays are traced backward to deep water from buoy sites D3 and D8. Slope of the $\theta^{(s)}$ vs $\theta^{(o)}$ relation (Gray dashed line shows 1-to-1 slope) indicates focusing (>1) and sheltering (<1). Missing rays indicate blocked (sheltered) directions. Integration at 1° resolution yields (b) energy transfer coefficients at buoy sites D3 and D8. Estimates at finely spaced frequencies (light shading, 0.0675–0.0725 Hz at 0.0005-Hz spacing) are averaged to represent each frequency band (dark lines).

$\tilde{\mathbf{H}}^{-g} = \tilde{\mathbf{H}}^T(\tilde{\mathbf{H}}\tilde{\mathbf{H}}^T)^{-1}$, the generalized inverse of the time-invariant version of the forward problem (i.e., time lags are neglected). For a perfectly resolved model $\text{res}(\tilde{\mathbf{H}}) = \mathbf{I}$, where **I** is the identity matrix. In most practical systems, the nonzero off-diagonal elements of $\text{res}(\tilde{\mathbf{H}})$ represent blurring of the true model solution (Parker 1994), while in a well-resolved system the diagonal values of $\text{res}(\tilde{\mathbf{H}})$ are near unity. Transfer coefficients for deep-water buoy sites D1–D8 (Fig. 3a), those with the longest records, are used
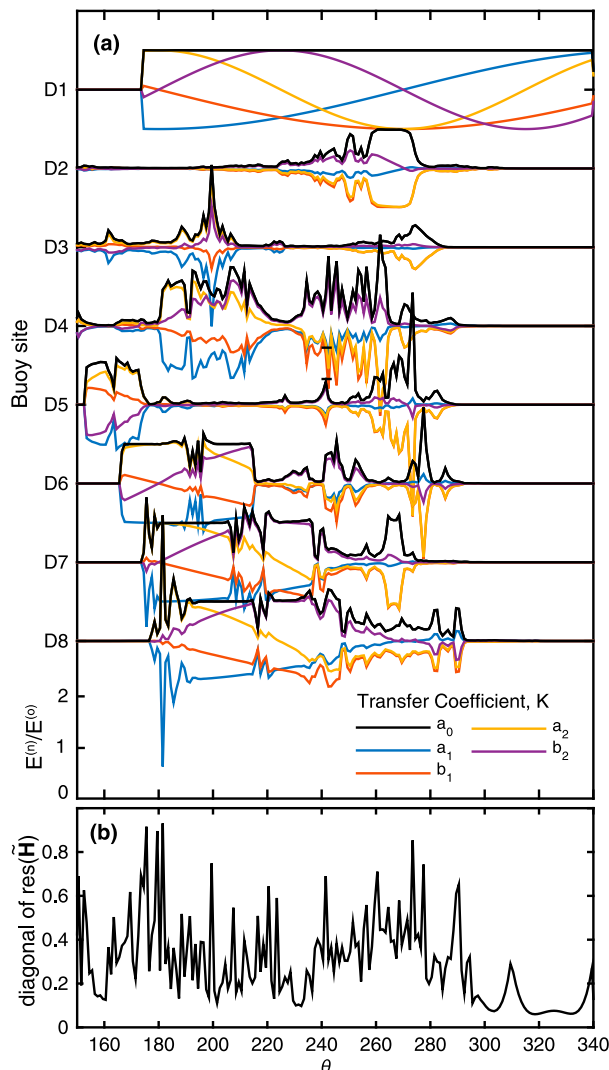
FIG. 3. (a) Time-invariant transfer coefficient vs offshore direction at deep-water SCB buoy sites (labeled) at the 0.07-Hz band for energy, a_o, (black), and directional moments: a_1 (blue), b_1 (red), a_2 (yellow), and b_2 (purple). (b) Diagonal values of resolution matrix, res($\tilde{\mathbf{H}}$), vs offshore direction.

to estimate res($\tilde{\mathbf{H}}$) (Fig. 3b). At 1° resolution, the diagonal values of res($\tilde{\mathbf{H}}$) vary widely, ranging from 0.2 to 0.8, with low values indicating blurring across directional bands. The available buoy array (D1–D8) has the highest theoretical resolution between 160°–180° and 240°–280°, where site transfer functions are most orthogonal. The theoretical resolution is low at directions >300° because only a single buoy site—D1—is exposed. While this procedure could determine the array with the best theoretical resolution, the important effects of observational uncertainty and forward model error are not captured.

In (5) wave energy travel times are neglected but are as large as 12 h in the ~350-km model domain. Time lags

$\tau(\theta)$ are estimated from great circle paths between the nearshore prediction site and the offshore wave energy front at buoy site D1 for each arrival direction (Fig. 4a) following previous studies (O'Reilly et al. 2016, Fig. B1). Lags are smallest when the line connects observation and prediction sites, and the wave propagation direction is parallel. A perpendicular line yields the largest lags. For southwest arrival directions lags are negative; the more southerly sheltered buoys lead the offshore buoy D1 (Fig. 4b). Although great circle lag estimates ignore details of actual ray paths, the differences are typically smaller than the model time step (1 h). Additionally, significant prediction errors in peak arrival timing were not observed.

Offshore wave energy is assumed to be homogeneous in the along-crest (alongfront) direction (Fig. 4a), a validated assumption in the SCB for frequencies <0.09 Hz (Crosby et al. 2016, appendix A). Though possible to allow heterogeneous wave conditions in the along-crest direction, the increase in boundary condition and forward problem complexity does not make a difference for low-frequency energy where this assumption holds.

Including time lags in (5) and assuming along-crest homogenous incoming energy fronts, the forward problem becomes

$$\tilde{\mathbf{y}}(i,t) = \int \mathbf{K}(i,\theta)E[\theta, t - \tau(\theta)]\,d\theta. \tag{7}$$

Predictions at any given time and nearshore location depend on offshore spectra at many recent times because waves at each frequency arrive from a range of directions (τ depends on θ). The time-dependent forward problem is discretized at 1-h time steps, and similar to (6) in matrix notation is

$$\mathbf{Hx} = \mathbf{y}, \tag{8}$$

where $\mathbf{H}$ contains buoy site transfer coefficients. Rows of $\mathbf{H}$ span nearshore locations, buoy-measured moments, and time steps, while columns span offshore directions and time steps, lagged appropriately by $\tau(\theta)$ (rounded to the nearest hour). The time-dependent forward problem [(8)] is that of O'Reilly and Guza (1998), but computational advances allow for higher estimates of directional (1°) and temporal (1 h) resolution of offshore spectra.

4. Inverse problem

The forward problem [(8)] is underdetermined and observations are noisy. Solutions are therefore non-unique (Ochoa and Delgado-González 1990; Parker 1994). A unique solution is obtained by minimizing the log-likelihood cost function (notation of Ide et al. 1997),
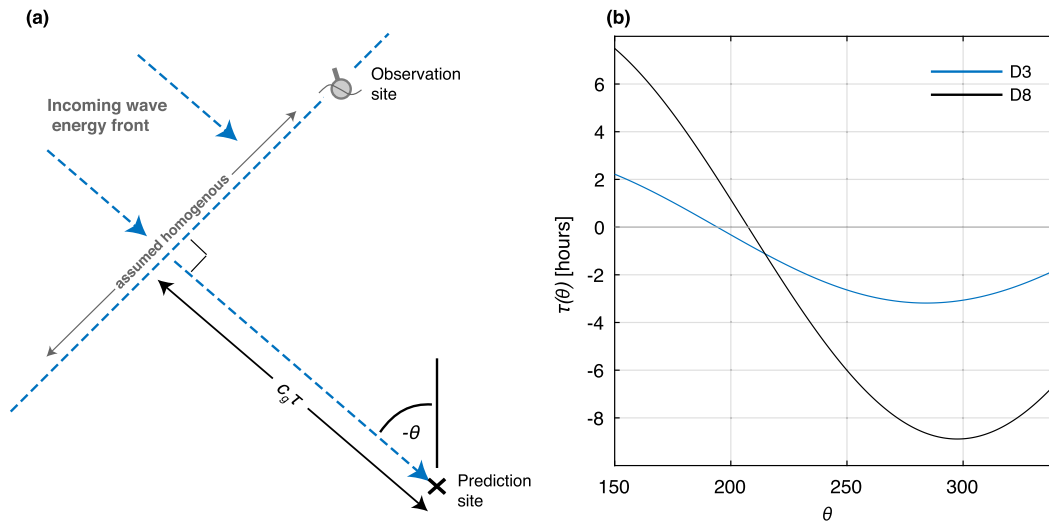
FIG. 4. (a) Schematic illustrating homogeniety assumption and time lag estimation between sites. (b) Time lag vs offshore direction for travel time between nearshore buoys D3 and D8 to offshore site D1 for 0.07-Hz energy. Note directions in Earth-relative compass coordinates.

$$\mathcal{J} = (\mathbf{H}\mathbf{x} - \mathbf{y})^{\mathrm{T}}\mathbf{R}^{-1}(\mathbf{H}\mathbf{x} - \mathbf{y}) + (\mathbf{x} - \mathbf{x}_p)^{\mathrm{T}}\mathbf{B}^{-1}(\mathbf{x} - \mathbf{x}_p), \tag{9}$$

and requiring nonnegative energy,

$$\mathbf{x} \geq 0. \tag{10}$$

The solution minimizes the squared sum of the normalized misfit to observations $\mathbf{y}$ and the normalized adjustments to model prior $\mathbf{x}_p$ (Wunsch 2006; Aster et al. 2013) under the assumption that observation and model prior uncertainty are normally distributed. The first rhs term of (9), the data misfit, is weighted by $\mathbf{R}^{-1}$, the data error covariance inverse. Term $\mathbf{R}$ is known for directional buoy observations (Long 1980; Borgman et al. 1982); however, off-diagonal data covariance terms are set to zero for simplicity (see the appendix), increasing the assumed observational uncertainty and likely biasing slightly the least squares solution. The second rhs term of (9) is the adjustment to the model prior, where $\mathbf{x}_p$ denotes the WW3 directional spectra predictions from the National Oceanic and Atmospheric Administration's 1979–2009 hindcast reanalysis (Tolman 2009; Chawla et al. 2013). Complete frequency-directional WW3 spectra at buoy site D1 are linearly interpolated to our model resolution (1° and 1 h) and are additionally linearly interpolated from their logarithmic frequency resolution to typical buoy swell-band resolution (0.005 Hz).

We posit that WW3 accurately predicts incoming wave directions because storm locations are well defined by satellite wind observations that drive global wave models. In contrast, model swell energies and detailed directional properties depend on many modeling approximations, and they may have significant error. Therefore, before specifying $\mathbf{x}_p$ with interpolated WW3 predictions, two adjustments are made using energy observed at offshore buoy site D1. First, for each 4-day case study, WW3 predictions are shifted in time to achieve maximum correlation with observed energy at buoy D1 (shifts in case examples are ≤3 h). Second, WW3 spectra energy at each f are adjusted to D1 observations.

The prior adjustment in (9) is weighted by the prior uncertainty covariance $\mathbf{B}$, where

$$\mathbf{B} = \mathbf{W}\mathbf{C}\mathbf{W}, \tag{11}$$

is constructed by weighting the model uncertainty correlation matrix $\mathbf{C}$ with the diagonal matrix $\mathbf{W}$, containing the standard deviations σ_x of $\mathbf{x}_p$ uncertainty. Although the uncertainty in WW3 bulk parameters can be estimated by comparison with buoy observations—for example, the RMSE of WW3 offshore θ_m in the SCB is ~10° for swell-band waves (Crosby et al. 2016)—the uncertainty of $\mathbf{x}_p$ at each directional bin is unknown.

The hypothesis of accurate WW3 predictions of peak wave directions is implemented by specifying σ_x with the convolution,

$$\sigma_x(\theta) = \alpha \int B(\theta') x_p(\theta - \theta') \, d\theta', \tag{12}$$
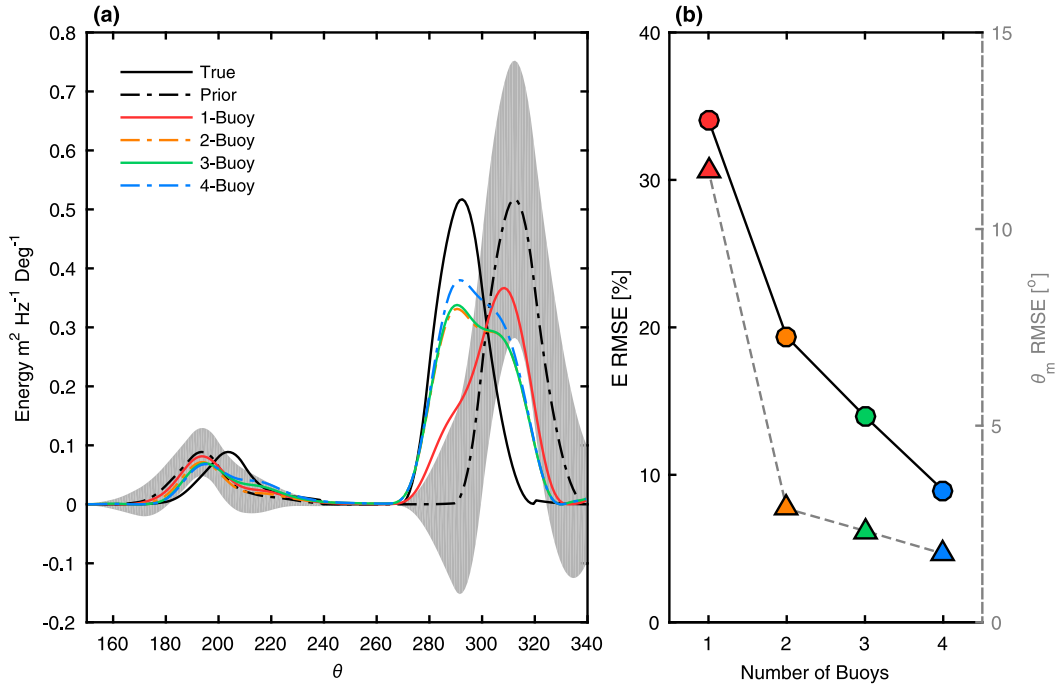
FIG. 5. Synthetic example of the assimilation technique: (a) energy vs direction at 0.06 Hz for plausible bimodal wave conditions. Synthetic observations are created with true spectra (black) run through the time-invariant forward problem [Eq. (6)] and perturbed by expected uncertainty in a 3-h record (see the appendix). Model prior (dashed–dotted line) and associated 1σ uncertainty (gray shading) are used with various combinations of synthetic buoys observations (refer to text) to solve for the offshore spectra (colored lines). (b) Prediction errors at validation sites (D2, D3, D4, D7, S2, S6) for offshore spectra estimates vs the number of buoys included in the estimate [colors correspond to spectra in (a)]. Shown are energy RMSE (%, solid black line) and θ_m RMSE (°, dashed gray line).

where α is a constant $O(1)$ and $B(\theta')$ is a boxcar,

$$B(\theta') = \begin{cases} 1/2L_B, & \text{if} \quad |\theta'| < L_B \\ 0, & \text{otherwise} \end{cases}. \quad (13)$$

In the limit $L_B = 1°$ (the model resolution), the uncertainty simply scales with the predicted energy level. However, with $L_B > 1$ the convolution in (12) increases uncertainty around the predicted peak direction and will ultimately allow the inversion to increased freedom to shift energy between directional bins. Values of $\alpha = 0.5$ and $L_B = 25°$ produced plausible uncertainties, for example, see the gray shading around the dotted–dashed spectrum in Fig. 5.

Model smoothness is specified in **C** by a Gaussian decay function,

$$C(\Delta\theta, \Delta t) = \exp\left[-\left(\frac{\Delta\theta}{L_\theta}\right)^2 - \left(\frac{\Delta t}{L_t}\right)^2\right]. \quad (14)$$

The decay constants L_θ and L_t define model smoothness scales in direction and time, respectively, and likely vary by frequency and storm location

(e.g., distant storms vs local seas). Decorrelation length scales, estimated from WW3 predictions {best fit to the Gaussian decay function [Eq. (14)]}, range from 10 to 30 h and from 16° to 20° with some dependence on frequency band (Fig. 6) but weak cross correlation between direction and time (not shown). Ultimately, weak sensitivity to decay constants was observed in our case examples (sections 5b, 6b).

Matrix **C** is challenging to invert because it is not diagonal, is often poorly conditioned, and is large ($O\,10^4 \times 10^4$) for a 4-day time span at 1-h and 1° resolution). The number of model parameters is reduced by transforming to a truncated orthogonal eigenvalue space. Though not computationally trivial, the decomposition of **C** is performed only once for each set of smoothing parameters L_θ, L_t needed. Matrix **C** is valid for any 4-day time span and is easily scaled by **W** to form **B**. Alternatively, decomposing **C** in time and direction independently significantly reduces computational demands (**C** is separable in these dimensions), and would allow for additional smoothness constraints across frequency and the assimilation of frequency-integrated observations, such as satellite altimeter H_s observations. In either case the
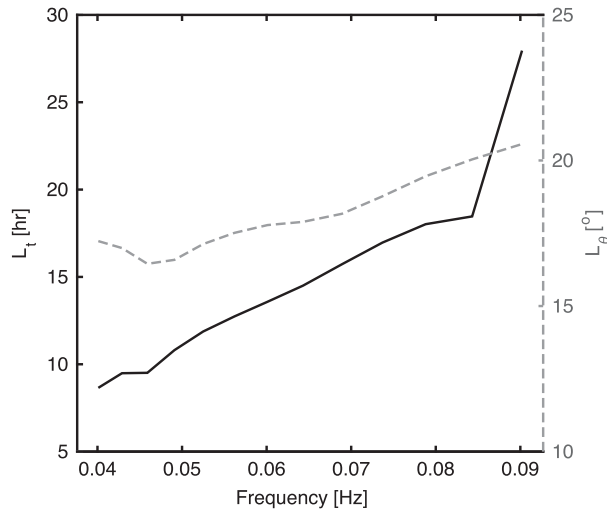
FIG. 6. WW3 time (solid line, left axis) and direction (dashed line, right axis) decorrelation length scales vs frequency. Decorrelation length scales are determined by best fit to Gaussian [Eq. (11)] of the WW3 autocorrelation function.

methodology remains the same: before truncation, the decomposition of $\mathbf{C}$ yields

$$\mathbf{C} = \mathbf{V}\mathbf{D}\mathbf{V}^{\mathrm{T}}, \tag{15}$$

where the diagonal matrix $\mathbf{D}$ contains eigenvalues and $\mathbf{V}$ contains the orthogonal eigenvectors. The model covariance matrix is now

$$\mathbf{B} = \mathbf{W}\mathbf{V}\mathbf{D}\mathbf{V}^{\mathrm{T}}\mathbf{W}, \tag{16}$$

with formal inverse,

$$\mathbf{B}^{-1} = \mathbf{W}^{-1}\mathbf{V}\mathbf{D}^{-1}\mathbf{V}^{\mathrm{T}}\mathbf{W}^{-1}, \tag{17}$$

where only diagonal matrices need be inverted. With $L_\theta \geq 25°$ and $L_t \geq 6\,\mathrm{h}$, solutions truncated after the largest 500 eigenvalues are accurate and are denoted with subscript k, where

$$\mathbf{B}_k^{-1} = \mathbf{W}^{-1}\mathbf{V}_k\mathbf{D}_k^{-1}\mathbf{V}_k^{\mathrm{T}}\mathbf{W}^{-1}. \tag{18}$$

The truncated $\mathbf{x}_k$ and original models are related by

$$\mathbf{x}_k = \mathbf{V}_k^{\mathrm{T}}\mathbf{W}^{-1}\mathbf{x} \quad \text{and} \quad \mathbf{x} = \mathbf{W}\mathbf{V}_k\mathbf{x}_k, \tag{19}$$

and truncated model kernel is similarly related,

$$\mathbf{H}_k = \mathbf{H}\mathbf{W}\mathbf{V}_k. \tag{20}$$

The cost function becomes

$$\mathcal{J} = (\mathbf{H}_k\mathbf{x}_k - \mathbf{y})^{\mathrm{T}}\mathbf{R}^{-1}(\mathbf{H}_k\mathbf{x}_k - \mathbf{y})$$
$$+ (\mathbf{x}_k - \mathbf{x}_{pk})^{\mathrm{T}}\mathbf{D}_k^{-1}(\mathbf{x}_k - \mathbf{x}_{pk}), \tag{21}$$

with the altered nonnegativity constraint,

$$\mathbf{W}\mathbf{V}_k\mathbf{x}_k \geq 0. \tag{22}$$

In equivalent form (Aster et al. 2013) minimization of

$$\left\| \begin{bmatrix} \mathbf{R}^{-1/2}\mathbf{H}_k \\ \mathbf{D}_k^{-1/2} \end{bmatrix} \mathbf{x}_k - \begin{bmatrix} \mathbf{R}^{-1/2}\mathbf{y} \\ \mathbf{D}_k^{-1/2}\mathbf{x}_{pk} \end{bmatrix} \right\|^2 \tag{23}$$

is rapid (5 min on a Pentium i7 4-core laptop) using quadratic programming techniques (MATLAB Optimization Toolbox). The numerical accuracy of the solution to (23) without the nonnegativity constraint [(22)] is confirmed by good agreement to the unconstrained analytical solution (Wunsch 2006),

$$\mathbf{x}^* = \mathbf{B}\mathbf{H}^{\mathrm{T}}(\mathbf{H}\mathbf{B}\mathbf{H}^{\mathrm{T}} + \mathbf{R})^{-1}\mathbf{y}. \tag{24}$$

The minimum solution to (21) with (22) was slightly negatively biased at the offshore buoy site D1 because event peak energies are consistently underpredicted owing to the smoothness constraint and proportionality of observed energy uncertainty to itself (see the appendix). The bias is corrected with the additional constraint that the event-averaged offshore inverse and observed energy (D1) match. This constraint is applied only at offshore site D1 because forward model errors and observational uncertainty preclude satisfaction at all buoy locations.

5. Case studies

a. Synthetic observations

A synthetic case study of the time-invariant forward problem (for simplicity) demonstrates that the minimum solution to (21) with (22) behaves as expected, given the forward model assumptions (e.g., linear wave propagation, along-crest homogeneity, and no wave reflection) are satisfied. A plausible offshore directional spectrum (inspired by WW3 predictions) is used to represent the true offshore energy distribution for an example frequency band, 0.06 Hz (solid black in Fig. 5a). The forward problem, $\tilde{\mathbf{H}}$, is created with the set of transfer coefficients at a synthetic buoy site using backward ray tracing. Synthetic buoy observations are generated using (6) with the true offshore spectrum and are perturbed randomly by the expected observational uncertainty for a 3-h buoy record at 0.005-Hz frequency resolution (see the appendix). Additionally, $\mathbf{x}_p$ is

TABLE 2. Mean RMSE of H_s and θ_m at validation buoy sites for each case study with WW3, INV, and MEM boundary conditions. INV solutions estimated with buoys D1, D5, D6, and D8 included in the inversion.

Case	Dates	Validation sites	Peak H_s (m)	Peak Freq (Hz)	RMSE – H_s (m)			RMSE – θ_m (°)		
					WW3	INV	MEM	WW3	INV	MEM
1	11–15 Jan 2004	D4, D7, D10, S3	3.0	0.06	0.27	0.13	0.18	6.5	3.0	4.3
2	20–24 Dec 2005	D4, D7, S1, S4	4.9	0.06	0.36	0.21	0.27	7.6	5.9	7.5
3	26–30 Dec 2006	D4, D7, D9, S1, S6	7.0	0.07	0.29	0.23	0.43	5.4	5.3	9.7
4	11–15 Jan 2008	D4, D7, D9, S2, S6	3.1	0.06	0.24	0.19	0.28	7.4	3.9	5.9
5	9–13 Feb 2008	D4, D7, D9, S2, S6	3.2	0.05	0.19	0.13	0.17	12.3	4.6	8.0
6	12–16 Nov 2008	D4, D7, D9, S5, S6	2.2	0.08	0.32	0.21	0.30	7.4	5.7	10.0

generated by shifting the true directional distribution (dashed–dotted line in Fig. 5a). The model covariance is estimated with $L_\theta = 25°$, $L_B = 25°$, and $\alpha = 0.5$, and is decomposed into an orthogonal eigenvalue space and truncated. Estimated offshore spectra, minimizing (21) with (22), are found using various combinations of synthetic buoy observations (and corresponding forward problem), specifically one buoy: D1; two buoys: D1, D5; three buoys: D1, D5, D6; and four buoys: D1, D5, D6, D8 (colored lines in Fig. 5a). As additional buoy observations are assimilated, solutions become increasingly similar to the true spectrum (despite relatively large directional error in $\mathbf{x}_p$) and prediction errors in energy and θ_m decrease compared to $\mathbf{x}_p$ predictions at nonassimilated (validation) synthetic buoy sites (D2, D3, D4, D7, S2, S6) (Fig. 5b).

b. Real observations

Case studies with real buoy observations demonstrate the assimilation method's skill in practice, where forward model assumptions are necessarily violated to some extent. Six moderate to large Pacific Northwest (NW) wave events were selected (Table 2), and various combinations of buoys were used in the assimilation. For simplicity, the additionally available offshore buoy observations, San Nicolas Island and Point Loma buoys (Fig. 1), used to drive CDIP's operational wave predictions (O'Reilly et al. 2016), are not included. Each 4-day period, bracketing the event, was analyzed at 1-h and 1° resolutions. The first and last 12 h of solutions to (21) are truncated to allow for complete propagation across the domain (e.g., 12-h travel time). For each wave event, inverse offshore spectra (INV) were found that minimize (21) with (22) using varying sets of regional buoy observations and adjusted WW3 predictions at buoy D1.

Tests with $L_\theta = 25°$, $L_t = 6$ h, $L_B = 25°$, and $\alpha = 0.5$, and all available buoy observations generated plausibly smooth offshore spectra, with modest adjustments to the model prior. For example, the INV spectrum at peak frequency in case 4 (Fig. 7c) is similar to the adjusted WW3 spectrum (Fig. 7b) but with more directional

asymmetry, increased temporal smoothness, and some additional features. The misfit between predictions by INV spectra (INV predictions) and buoy observations used in the minimization are generally small (right panels of Fig. 7). Notable exceptions are buoys D2 and S2, where peak observed wave energy is more than twice that predicted by INV and WW3.

INV spectra with smoothing constants as above and all available buoy observations (availability varies with the case study; Table 2) are generated for all cases at all swell-band frequencies. Frequency-integrated and time-averaged observed and INV-predicted energies (Fig. 8) show good agreement in many cases, but they highlight a particularly severe bias (misfits up to three standard deviations) at buoys D2 and D3, both located in the eastern half of the Santa Barbara Channel (Fig. 1). These deep-water buoys are highly sheltered from NW swell by Point Conception, and we hypothesize forward model errors are large. Relaxation of smoothness constraints—for example, $L_\theta = 10°$ and $L_t = 3$ h—improved fits negligibly (not shown) and suggest that no plausibly smooth spectrum exists that can fit all observations within their uncertainty. Santa Barbara Channel nearshore buoys S1 and S2 are also biased low (Fig. 8) and the persistent negative bias in the region suggests that additional energy may be directed into the Santa Barbara Channel by diffraction around Point Conception, reflection off the Channel Islands, or refraction by surface currents. Additionally, previous studies suggest waves in the SBC are difficult to model accurately (Rogers et al. 2007; O'Reilly et al. 2016; Crosby et al. 2016). Buoy S4, located just offshore of Huntington Beach, is also poorly fit in case 2, but more cases are needed to determine whether there is systematic forward model error at this site.

6. Discussion

a. Assimilation method skill

Nearshore prediction skill can likely be improved by corrections to the forward model physics, but only
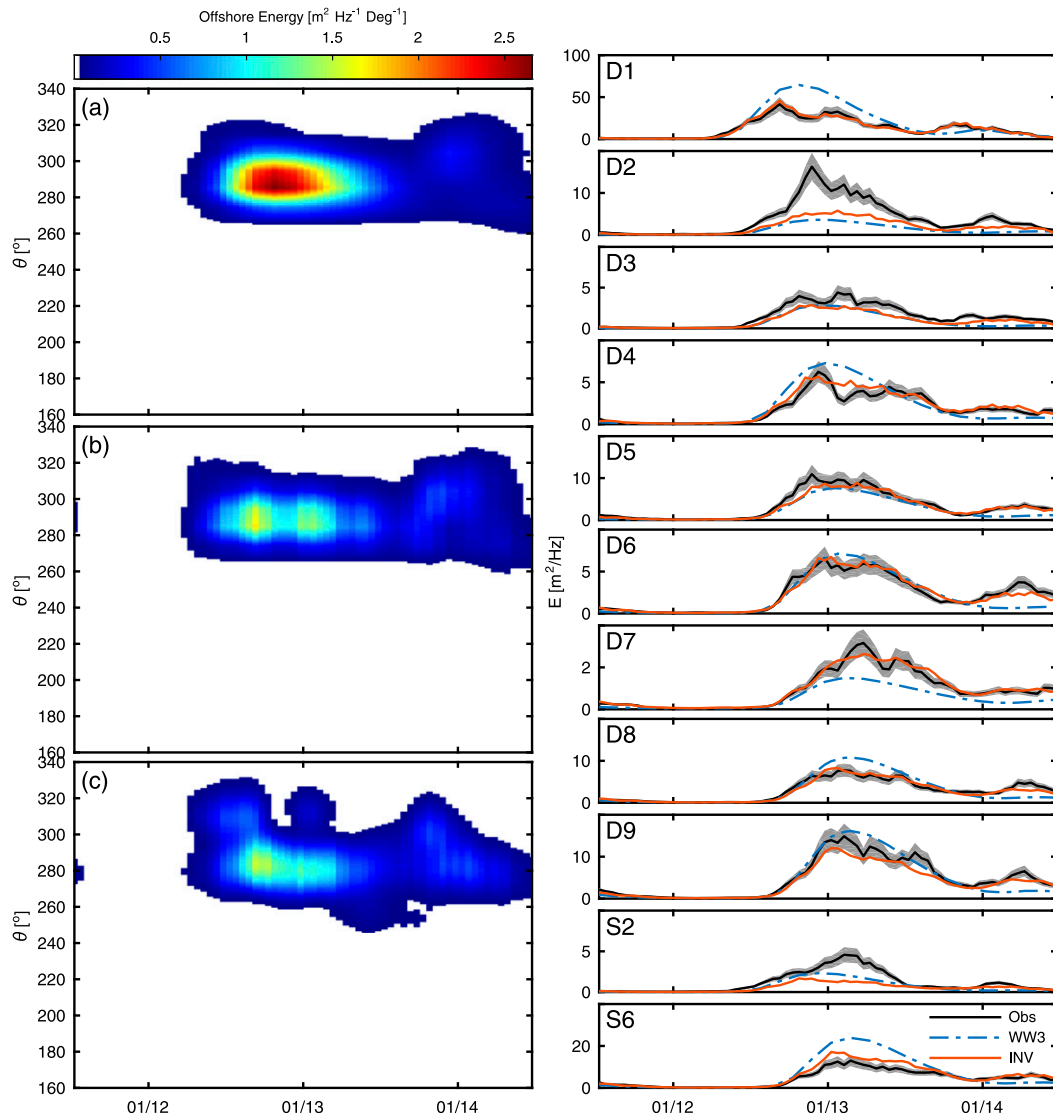
FIG. 7. (left) Offshore directional spectra and (right) energy observations and predictions at buoy sites vs time at the 0.06-Hz swell-band frequency for a wave event during January 2008 (case 4). Gray shading indicates observational uncertainty at the 95% confidence level. (a) WW3 spectra, (b) WW3 spectra are shifted 1 h backward in time and adjusted to match total energy observed at buoy D1, and (c) INV spectra generated using all buoy observations (left) and adjusted WW3 spectra in the minimization of (23) with $L_t = 6$ h, $L_\theta = 25°$, $\alpha = 0.5$, and $L_B = 25$. The largest misfits to buoys D2 and S2 are likely owing to forward model errors in the eastern SBC.

boundary condition corrections are considered here. Buoys D2 and D3 are excluded from the following analysis because of large forward model error. Assimilation of these sites may degrade boundary condition corrections and increase prediction errors at other locations. The skill of INV solutions with selected assimilated sites (D1, D5, D6, D8) is assessed with comparisons of predictions and observations at non-assimilated (validation) buoy locations. By design, improvement is expected at assimilated buoy sites (Fig. 7); however, skill improvement at validation sites

suggests that the INV offshore spectrum is increasingly accurate and that prediction skill improvement is regionwide. For all cases, assimilation improves skill for swell-band-integrated bulk wave parameters, H_s and θ_m (Table 2). Both H_s and θ_m RMSEs are reduced by 20%–50% relative to WW3 when buoys sites D1, D5, D6, and D8 are assimilated. Assimilated model skill is also higher than predictions made with observations at D1 and the maximum entropy method (MEM; Lygre and Krogstad 1986), a commonly used technique to estimate directional spectra from buoy directional
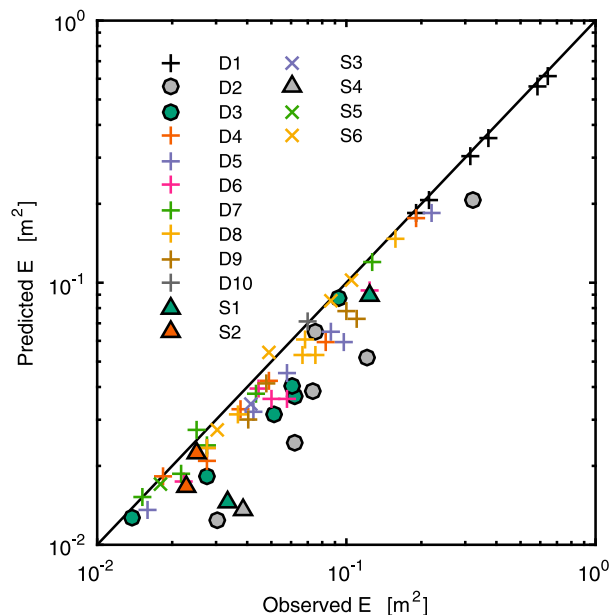
FIG. 8. Predicted vs observed E, integrated across swell frequency bands and temporally averaged, for each case study. Predictions with INV solutions use all available buoy observations. Some observations are not well fit by the INV methods and indicate forward model errors, e.g., D2, D3, S1, S2, and S4.

moments. MEM is currently used in CDIP's operational wave but with a heuristic blend of multiple offshore buoy observations (O'Reilly et al. 2016). Here, INV predictions are overall most highly skilled, followed by MEM and WW3 predictions.

b. Model prior, **B**

The model prior and model covariance uncertainty select a solution from a theoretically infinite set by imposing desired characteristics, for example, smoothness and similarity to a preferred model. Smoothness is set by **C**, parameterized by a Gaussian decay function [(14)], with two adjustable parameters, L_θ and L_t. WW3 spectra predictions suggest that decorrelation length scales in time and direction increase slightly with frequency and range from 10 to 28 h and from 16° to 21° (Fig. 6). The trend in temporal decorrelation scale may appear counterintuitive, as low-frequency energy from distant storms may persist for days, whereas local-generated seas vary over hours. However, owing to the dispersion of low-frequency energy over long travel distances, energy at very low frequency (e.g., 0.05 Hz) decorrelates more quickly than high frequencies (e.g., 0.09 Hz).

INV solutions were generally insensitive to variations over the following parameter ranges: $10° \leq L_\theta \leq 40°$, $3 h \leq L_t \leq 18 h$, $0.25 \leq \alpha \leq 1$, and $25° \leq L_B \leq 50°$. Ultimately, $L_\theta = 25°$ was chosen because it yielded slightly higher prediction skill, $L_t = 6 h$ because it agreed well

with time scales in regional buoy observations, and $L_B = 25°$ and $\alpha = 0.5$ because the specified model prior uncertainty appeared plausible (e.g., Fig. 5). Optimal parameter values vary by frequency and event, and variable parameter values were also considered; L_θ was set on an event-by-event, frequency-by-frequency basis to the directional decorrelation of WW3 predictions. However, changes in INV skill were small.

The model prior uncertainty σ_x controls the influence of WW3 predictions in the INV solution. Previous studies, with an effectively constant σ_x, were plagued with spurious directional peaks from unlikely directions (Long and Hasselmann 1979; Crosby et al. 2016). The present σ_x parameterization [(12)] harshly penalizes energy far from peak energy in WW3 predictions (note the lack of spurious energy in Fig. 7c). Improved estimates of σ_x would undoubtedly help constrain offshore wave conditions in regional assimilations but require a high-resolution ground truth.

The assumption of Gaussian statistics throughout the inversion framework makes the search for a solution within a large model space computationally feasible. Although buoy-measured moments [(1)] are χ^2 distributed, for the present high degrees of freedom (196 given 3-h 0.005-Hz data; see the appendix) the χ^2 distribution is well approximated as Gaussian. Gaussian uncertainty is formally inconsistent with the nonnegativity on the INV solutions (e.g., gray shading of uncertainty in Fig. 5). However, the effect is likely small because solutions without the nonnegativity constraint in (24) contained relatively small amounts of negative energy (~10%).

c. Implications for buoy array design

An optimal operational array balances buoy value and cost. Buoy costs depend on ease of servicing, mooring depth, exposure to shipping and fishing, and other factors. Buoy value depends on site-specific local factors (e.g., nearby port), and more generally on the improvement in local and regional model skill. Offshore buoys are of primary importance to regional prediction, providing unsheltered deep-water observations free from forward model errors and several hours before waves arrive at the coast. Energy travel time lags in the SCB vary with wave direction, and both a southerly located buoy (e.g., Point Loma) and a northerly located buoy (e.g., Harvest) are needed to provide nowcast and short-term forecast predictions (O'Reilly et al. 2016). In smaller regions one offshore buoy may be sufficient. Nearshore buoy locations have historically been determined by funding sources and local community needs. Assimilation methods estimate the overall added predictive skill and help assess optimal buoy placement.
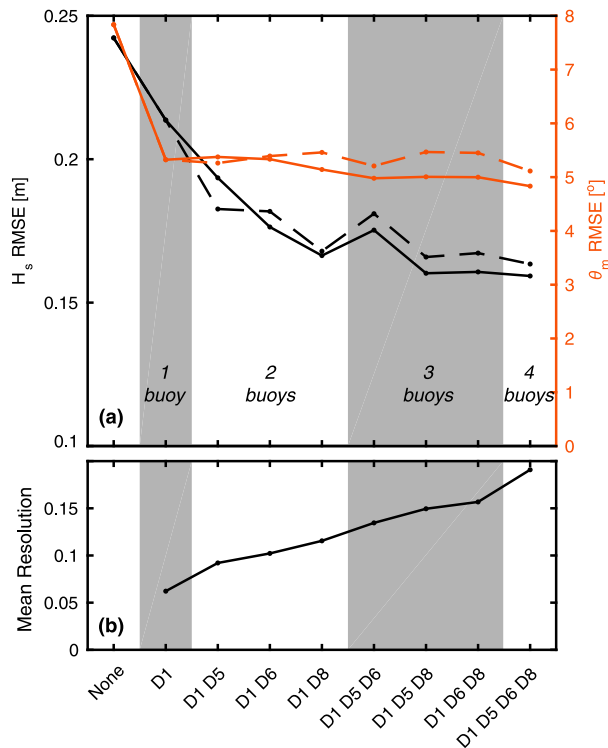
FIG. 9. The (a) H_s (black, left axis) and θ_m (red, right axis) RMSE of INV predictions at specified validation sites (Table 2) averaged across all cases vs varying combinations of assimilated buoy observations ($L_t = 6$ h, $L_\theta = 25°$, $\alpha = 0.5$, and $L_B = 25$). "None" corresponds to the unadjusted WW3 prediction and has the largest errors. Solid lines show assimilation of nearshore buoy observations, including directional moments, while dashed lines show assimilation of only nearshore buoy energy observations. Overall error is reduced with additional buoy observations, and assimilation of nearshore directional observations have minimal impact. (b) Mean of the res($\tilde{\mathbf{H}}$) diagonal weighted by the 2000–09 WW3 offshore spectra climatology for the given buoy array (x axis).

Our case studies are not comprehensive, but initial analysis suggests that assimilation of nearshore buoy D8 yields the largest improvement in overall swell prediction (mainly H_s), given that offshore buoy D1 is included (Fig. 9a). Both H_s and θ_m RMSE are reduced at validation sites as additional buoy observations are assimilated (Fig. 9a), and these incremental improvements help quantify the value of each additionally buoy. Here, H_s RMSE reduction is negligibly small after buoys D1 and D8 are assimilated, and θ_m RMSE reduction is negligible after D1 is assimilated.

Accurate unbiased directional buoy observations have historically been difficult and expensive to acquire. Some buoy directional moments contained bias (e.g., the National Data Buoy Center 3-m discus; O'Reilly et al. 1996). More recently inexpensive GPS

sensors have been shown to yield accurate energy spectra and second-order directional moments but poorly resolve vertical motions, resulting in biased first-order directional moments (Herbers et al. 2012). While the high value of accurate offshore directional moments for regional swell prediction is clear (O'Reilly et al. 2016; Crosby et al. 2016), our analysis suggests less value for nearshore directional information. RMSE errors for INV predictions generated with and without assimilation of nearshore directional buoy observations are similar (Fig. 9a). Note that directional observations from offshore buoy D1 are included in both inversions. Regional skill is most efficiently improved by D1 energy and directional observations, and D8 energy observations. The negligible improvement in regional skill by nearshore directional information may be attributed to 1) the lack of shoreline reflection in the forward model (shoreline incident energy is assumed to completely dissipate) that affects directional observations significantly more than energy (Herbers et al. 1999; Crosby et al. 2016); and/or 2) increasingly sheltered regions' directional observations becoming nearly redundant to energy observations because waves arrive from a single known direction. The only useful information is the magnitude and timing of arriving energy; the arrival direction is already known. Although adding relatively little to regional swell prediction (given the nonreflective, linear forward model), directional nearshore observations may provide useful local wave information, for example, providing robust estimates of local radiation stress (Longuet-Higgins and Stewart 1964).

Theoretically, additional buoy observations add the most skill to regional swell prediction when their offshore transfer functions (Fig. 3) are most unique, providing additional constraints on the offshore spectrum. The mean array resolution (Fig. 9b) is estimated by averaging the res($\tilde{\mathbf{H}}$) diagonal weighted by the 2000–09 WW3 offshore spectra climatology (resolving power is needed most at the most common arrival directions). Perhaps fortuitously, the mean resolution indicates the largest theoretical improvement from buoy D8 given D1, the same result observed in the case studies with real observations. This analysis focuses on existing buoy sites, applicable to identifying redundant observations and regions of significant forward model error. If the forward model is trusted, then ideal buoy sites could be determined by the added theoretical resolution, similar to O'Reilly and McGehee (1994). However, the forward model fails in some locations (e.g., east end of SBC). Short-term buoy deployment (e.g., 1–2 years) at selected sites could identify regions where the forward

model succeeds and fails, and where local observations add the most value to swell prediction regionwide. This application of our inverse methods is preliminary; the incorporation of multiple offshore buoy sites, the addition of shoreline reflection (Ardhuin and Roland 2012), and the comprehensive analysis of additional observations are needed.

7. Summary

We developed methods to improve nearshore swell-band wave prediction by assimilating nearshore directional buoy observations of frequency spectra and offshore global wave model (GWM) spectra predictions. Assimilation yields accurate high-resolution (direction and time) offshore wave spectra and accurate high-resolution (space and time) coastal wave predictions. Methods use linear (shoaling and refraction) wave propagation assumptions, valid on narrow continental shelves—for example, the U.S. West Coast—at swell-band frequencies (0.04–0.09 Hz). The linear wave energy propagation model, generated with backward ray tracing techniques, requires minimal computation and enables relatively rapid assimilation (compared to 4DVAR techniques). Regional prediction skill improvements are relatively insensitive to user-determined constraints. Nearshore buoy observations poorly fit by assimilated offshore spectra identify sites where significant wave physics are likely missing from the linear forward model. Overall, regional swell prediction errors are reduced by approximately 30% when observations are assimilated, and incremental improvements become insignificant after two to three buoys are assimilated. Varying the buoy observations included in the assimilation provides insight into optimal array design for regional nearshore swell prediction. The Bayesian framework of the assimilation advantageously incorporates prior information easily, for example, offshore GWM spectra predictions. Future improvements to GWM predictions, and an improved understanding of their uncertainty, will ultimately improve regional prediction skill. Though methods are restricted to regions and frequencies where wave propagation is approximately linear, these computationally rapid methods could be incorporated into a larger assimilation scheme, providing estimates for low-frequency energy and/or a first guess for more sophisticated nonlinear techniques.

APPENDIX

Observation Uncertainty

Buoy observations $\tilde{\mathbf{y}}$ are derived from cross spectra of vertical and horizontal translations. Typically, directional moments (a_1, b_1, a_2, b_2) are normalized to reduce instrument gain errors (Long 1980); however, here unnormalized moments are used such that

$$\tilde{\mathbf{y}} = \begin{bmatrix} a_0 \\ a_1 \\ b_1 \\ a_2 \\ b_2 \end{bmatrix} = \begin{bmatrix} S_{zz} \\ Q_{zx} \\ Q_{zy} \\ S_{xx} - S_{yy} \\ 2C_{xy} \end{bmatrix}, \qquad \text{(A1)}$$

where S, C, Q are power spectra, cospectra, and quad spectra of buoy translations in vertical (z) and horizontal (x, y) motions, respectively (Longuet-Higgins et al. 1963). The variance of $\tilde{\mathbf{y}}$ is then (Bendat and Piersol 1971)

$$\text{var}(\tilde{\mathbf{y}}) = \frac{1}{\sqrt{n_d}} \begin{bmatrix} S_{zz}^2 \\ \frac{1}{2}(S_{zz}S_{xx} + Q_{zx}^2) \\ \frac{1}{2}(S_{zz}S_{yy} + Q_{zy}^2) \\ S_{xx}^2 + S_{yy}^2 - \gamma_{xy}^2 S_{xx}S_{yy} \\ 2(S_{xx}S_{yy} + C_{xy}^2) \end{bmatrix}, \qquad \text{(A2)}$$

where $2 \times n_d$ = degrees of freedom and γ is the signal coherence. At 0.005-Hz frequency resolution and 3-h smoothed temporal resolution, $n_d = 48$. Onboard Datawell buoy processing slightly smooths observations across frequencies, increasing the degrees of freedom ($n_d = 96$). Note, however, the neighboring frequency-band observations are no longer statistically independent. Covariances between buoy moments are known (Long 1980; Borgman et al. 1982), but they are ignored for computational simplicity. This simpler diagonal $\mathbf{R}$ tends to overestimate actual observational uncertainty.

REFERENCES

Ardhuin, F., and A. Roland, 2012: Coastal wave reflection, directional spread, and seismoacoustic noise sources. *J. Geophys. Res.*, **117**, C00J20, doi:10.1029/2011JC007832.

Aster, R. C., B. Borchers, and C. H. Thurber, 2013: *Parameter Estimation and Inverse Problems.* Academic Press, 360 pp.

Bendat, J. S., and A. G. Piersol, 1971: *Random Data: Analysis and Measurement Procedures.* 4th ed. Wiley, 604 pp.

Borcea, L., G. Papanicolaou, C. Tsogka, and J. Berryman, 2002: Imaging and time reversal in random media. *Inverse Probl.*, **18**, 1247, doi:10.1088/0266-5611/18/5/303.

Borgman, L. E., R. L. Hagan, and A. J. Kuik, 1982: Statistical precision of directional spectrum estimation with data from a tilt-and-roll buoy. *Topics in Ocean Physics: Proceedings of Course LXXX at the International Schools of Physics*, A. R. Osborne and P. Malanotte Rizzoli, Eds., North-Holland, 418–438.

Chawla, A., D. M. Spindler, and H. L. Tolman, 2013: Validation of a thirty year wave hindcast using the Climate Forecast System Reanalysis winds. *Ocean Modell.*, **70**, 189–206, doi:10.1016/j.ocemod.2012.07.005.

Crosby, S. C., W. C. O'Reilly, R. T. Guza, S. C. Crosby, W. C. O'Reilly, and R. T. Guza, 2016: Modeling long-period swell in Southern California: Practical boundary conditions from buoy observations and global wave model predictions. *J. Atmos. Oceanic Technol.*, **33**, 1673–1690, doi:10.1175/JTECH-D-16-0038.1.

Dorrestein, R., 1960: Simplified method of determining refraction coefficients for sea waves. *J. Geophys. Res.*, **65**, 637–642, doi:10.1029/JZ065i002p00637.

García-Medina, G., H. T. Özkan-Haller, P. Ruggiero, and J. Oskamp, 2013: An inner-shelf wave forecasting system for the U.S. Pacific Northwest. *Wea. Forecasting*, **28**, 681–703, doi:10.1175/WAF-D-12-00055.1.

Herbers, T. H. C., S. Elgar, and R. T. Guza, 1999: Directional spreading of waves in the nearshore. *J. Geophys. Res.*, **104**, 7683–7693, doi:10.1029/1998JC900092.

——, P. F. Jessen, T. T. Janssen, D. B. Colbert, and J. H. MacMahan, 2012: Observing ocean surface waves with GPS-tracked buoys. *J. Atmos. Oceanic Technol.*, **29**, 944–959, doi:10.1175/JTECH-D-11-00128.1.

Ide, K., P. Courtier, M. Ghil, and A. C. Lorenc, 1997: Unified notation for data assimilation: Operational, sequential and variational. *J. Meteor. Soc. Japan*, **75**, 181–189, doi:10.2151/jmsj1965.75.1B_181.

Kuik, A. J., G. P. van Vledder, L. H. Holthuijsen, A. J. Kuik, G. P. van Vledder, and L. H. Holthuijsen, 1988: A method for the routine analysis of pitch-and-roll buoy wave data. *J. Phys. Oceanogr.*, **18**, 1020–1034, doi:10.1175/1520-0485(1988)018<1020:AMFTRA>2.0.CO;2.

Long, R. B., 1980: The statistical evaluation of directional spectrum estimates derived from pitch/roll buoy data. *J. Phys. Oceanogr.*, **10**, 944–952, doi:10.1175/1520-0485(1980)010<0944:TSEODS>2.0.CO;2.

——, and K. Hasselmann, 1979: A variational technique for extracting directional spectra from multi-component wave data. *J. Phys. Oceanogr.*, **9**, 373–381, doi:10.1175/1520-0485(1979)009<0373:AVTFED>2.0.CO;2.

Longuet-Higgins, M. S., 1957: On the transformation of a continuous spectrum by refraction. *Math. Proc. Cambridge Philos. Soc.*, **53**, 226–229 doi:10.1017/S0305004100032163.

——, and R. Stewart, 1964: Radiation stresses in water waves; a physical discussion, with applications. *Deep-Sea Res. Oceanogr. Abstr.*, **11**, 529–562, doi:10.1016/0011-7471(64)90001-4.

——, D. Cartwright, and N. Smith, 1963: Observations of the directional spectrum of sea waves using the motions of a floating buoy. *Ocean Wave Spectra: Proceedings of a Conference*, Prentice-Hall, 111–136.

Lygre, A., and H. E. Krogstad, 1986: Maximum entropy estimation of the directional distribution in ocean wave spectra. *J. Phys. Oceanogr.*, **16**, 2052–2060, doi:10.1175/1520-0485(1986)016<2052:MEEOTD>2.0.CO;2.

O'Reilly, W. C., and R. T. Guza, 1993: A comparison of two spectral wave models in the Southern California Bight. *Coastal Eng.*, **19**, 263–282, doi:10.1016/0378-3839(93)90032-4.

——, and D. D. McGehee, 1994: Design of regional wave monitoring networks: A case study for the Southern California Bight. U.S. Army Corps of Engineers Tech. Rep., 46 pp.

——, and R. T. Guza, 1998: Assimilating coastal wave observations in regional swell predictions. Part I: Inverse methods. *J. Phys. Oceanogr.*, **28**, 679–691, doi:10.1175/1520-0485(1998)028<0679:ACWOIR>2.0.CO;2.

——, T. H. C. Herbers, R. J. Seymour, and R. T. Guza, 1996: A comparison of directional buoy and fixed platform measurements of Pacific swell. *J. Atmos. Oceanic Technol.*, **13**, 231–238, doi:10.1175/1520-0426(1996)013<0231:ACODBA>2.0.CO;2.

——, C. B. Olfe, J. Thomas, R. Seymour, and R. Guza, 2016: The California coastal wave monitoring and prediction system. *Coastal Eng.*, **116**, 118–132, doi:10.1016/j.coastaleng.2016.06.005.

Ochoa, J., and O. E. Delgado-González, 1990: Pitfalls in the estimation of wind wave directional spectra by variational principles. *Appl. Ocean Res.*, **12**, 180–187, doi:10.1016/S0141-1187(05)80025-2.

Orzech, M. D., J. Veeramony, H. Ngodock, M. D. Orzech, J. Veeramony, and H. Ngodock, 2013: A variational assimilation system for nearshore wave modeling. *J. Atmos. Oceanic Technol.*, **30**, 953–970, doi:10.1175/JTECH-D-12-00097.1.

Panteleev, G., M. Yaremchuk, and W. E. Rogers, 2015: Adjoint-free variational data assimilation into a regional wave model. *J. Atmos. Oceanic Technol.*, **32**, 1386–1399, doi:10.1175/JTECH-D-14-00174.1.

Parker, R. L., 1994: *Geophysical Inverse Theory.* Princeton Series in Geophysics, Princeton University Press, 386 pp.

Rogers, W. E., J. M. Kaihatu, L. Hsu, R. E. Jensen, J. D. Dykes, and K. T. Holland, 2007: Forecasting and hindcasting waves with the SWAN model in the Southern California Bight. *Coastal Eng.*, **54**, 1–15, doi:10.1016/j.coastaleng.2006.06.011.

Tolman, H. L., 2009: User manual and system documentation of WAVEWATCH III version 3.14. NOAA Tech. Rep., 220 pp. [Available online at http://polar.ncep.noaa.gov/mmab/papers/tn276/MMAB_276.pdf.]

Veeramony, J., D. Walker, and L. Hsu, 2010: A variational data assimilation system for nearshore applications of SWAN. *Ocean Modell.*, **35**, 206–214, doi:10.1016/j.ocemod.2010.07.008.

Walker, D. T., 2006: Assimilation of SAR imagery in a nearshore spectral wave model. Office of Naval Research Tech. Rep., 39 pp.

Wunsch, C., 2006: *Discrete Inverse and State Estimation Problems: With Geophysical Fluid Applications.* Cambridge University Press, 371 pp.